Journal of Nuclear Materials 400 (2010) 112–118

Contents lists available at ScienceDirect

Journal of Nuclear Materials

journal homepage: www.elsevier.com/locate/jnucmat

Oxygen diffusion in relation to p-type doping in uranium dioxide

P. Garcia [a,*], M. Fraczkiewicz [a], C. Davoisne [a,c], G. Carlot [a], B. Pasquet [a], G. Baldinozzi [b], D. Siméone [b], C. Petot [b]

[a] CEA, DEN, DEC, St-Paul-Lez-Durance Cedex 13108, France
[b] Matériaux fonctionnels pour l'énergie, équipe mixte CEA-CNRS-ECP, Gif-Sur-Yvette 91191, France
[c] Laboratoire de Réactivité et Chimie des Solides UPJV, Hellemmes-Lille 59260, France

ARTICLE INFO

Article history:
Received 15 September 2009
Accepted 23 February 2010

ABSTRACT

In this paper we show how electrical conductivity and intrinsic oxygen diffusion coefficient measurements can be used in conjunction to further our understanding of oxygen related point defects in UO_2. Electrical conductivity measurements have enabled an estimate to be made of the positive charge carrier concentration in two sets of samples containing different levels of doping agents. The gas–solid isotopic exchange method was then used to load the samples with ^{18}O tracer atoms the concentration profile of which were subsequently characterised using SIMS and chromatic confocal microscopy. At the oxygen potential and temperature studied (750 °C), application of point-defect theory to our experimental results points to oxygen migration proceeding via an interstitial mechanism and to the fact that impurities control the concentration of negatively charged point defects responsible for atomic migration.

© 2010 Elsevier B.V. All rights reserved.

1. Introduction

Thermally or radiation induced transport properties impact practically all engineering aspects of nuclear oxide fuels, whether at the manufacturing stage, during in-reactor operation, or under long-term repository conditions. From a more fundamental standpoint, measuring transport properties is also a means of probing point or complex defects that are responsible for atomic migration: it is the starting point for developing a physically based thermodynamic model capable of describing the dependence of the material's deviation from stoichiometry upon the equilibrium oxygen potential [1]. Although many studies relating to oxygen diffusion in UO_2 have been carried out in the past 40 years (see for instance [2] for a review of self-diffusion properties of UO_2 along with [3] for more recent work relating specifically to oxygen diffusion), none has ever focussed on characterising this property as a function of all the physical variables which determine it, i.e. temperature and composition; the latter variable being determined, depending upon the temperature range investigated, by the equilibrium oxygen partial pressure and the concentration of bi- or tri-valent impurities inevitably present on the cation sublattice.

Following work done in the past on non-stoichiometric oxide compounds [4,5], we wish to ascertain the mass balance equations which govern point defect concentration levels in the material. It is the aim of this work to show how a systematic study of the dependence upon oxygen potential of electrical conductivity and oxygen diffusion properties can provide data characteristic of the nature and properties of point defects responsible for oxygen movement.

We first describe the two types of materials studied along with the experimental techniques employed to characterise them. The results relating to both electrical conductivity and ^{18}O depth profile characterisations are then presented. The data are subsequently interpreted and discussed at length.

2. Experimental

2.1. Sample preparation and characterisation

Two types of materials were used in this study. The first pertains to high density polycrystalline samples. The samples were obtained from sintered pellets (roughly 98% of theoretical density). The pellets were cut into wafers approximately 2 mm thick for the ^{18}O diffusion experiments, polished and subsequently annealed at 1700 °C for 80 h. The grain size following this heat treatment was estimated at approximately 24 ± 11 μm. The electrical conductivity specimen was obtained in exactly the same way and then cut into a bloc prior to annealing $6.1 \times 2.6 \times 2.5\ mm^3$ in size. The material the samples of the second set were made out of was obtained upon cooling of a mass of molten uranium dioxide and zirconium alloy. Chemical analyses revealed no zirconium contamination of the samples. Samples were then cut into slabs and polished appropriately, ready for annealing and subsequent SIMS or electrical conductivity characterisation.

* Corresponding author. Tel.: +33 4 42 25 41 88; fax: +33 4 42 25 13 37.
E-mail addresses: philippe.garcia@cea.fr (P. Garcia), mathieu.fraczkiewicz@cea.fr (M. Fraczkiewicz).

0022-3115/$ - see front matter © 2010 Elsevier B.V. All rights reserved.
doi:10.1016/j.jnucmat.2010.02.019

2.2. Electrical conductivity measurements

The classic four point Kelvin Double Bridge method [6,7] was used for electrical conductivity measurements which were established as a function of temperature, after the samples, placed in a flowing gas mixture of pure Ar and Ar/10% H_2, had reached a state of thermodynamic equilibrium. The dependence upon oxygen potential of the single crystals' electrical conductivity was also looked at. The higher oxygen potentials were obtained by making the Ar/10% H_2 gas mixture flow through a receptacle containing demineralised water. Ar and Ar/H_2 flow rates were adjusted so as to reach the desired oxygen potentials which were measured using a zirconia oxygen probe.

The current frequency used was 1.5 kHz and the bridge equilibrium was monitored using a fast detection amplifier. The conductivity of the sample is simply obtained from the measurement of the resistance of the sample and the sample geometry (section and length). Electrical conductivity measurements were performed over temperatures ranging between 340 °C and 1000 °C for the polycrystalline sample and between 1000 °C and 1300 °C for the single crystal sample. For this latter type of sample, a systematic study as a function of temperature and oxygen potential was performed in order to illustrate the transition from an extrinsic to intrinsic regime, whereas for the polycrystalline sample, a study as a function of temperature only and at the lowest possible oxygen partial pressure was carried out. Oxygen partial pressures ranged between *ca.* 10^{-22} atm and 10^{-9} atm for the lowest temperatures and *ca.* 10^{-16} atm and 10^{-5} atm for the highest temperatures.

2.3. Annealing treatments

Oxygen diffusion measurements rely upon an ^{18}O tracer protocol involving a solid–gas isotopic exchange at the surface of samples [5]. An alumina furnace was used. The single crystal and polycrystalline samples were placed in a small platinum sample holder and annealed simultaneously. The sample holder was attached to the end of a mobile alumina rod placed inside a quartz tube which enabled the samples to be inserted rapidly in the relevant region of the furnace, thus minimising the time it took for the sample to reach the desired temperature. The Ar/10% H_2 carrier gas used for the annealing experiment passes through one of two receptacles both containing demineralised water but with an ^{18}O enrichment of either 0.2% or 98%. The carrier gas thus loads itself with water (maintained at 5 °C) at the corresponding equilibrium vapour pressure.

Annealing proceeds in two stages. Stage 1 begins with the samples being placed in the hot region of the furnace once the desired temperature and oxygen potential are reached. During this stage, referred to hereafter as the pre-annealing stage, the carrier gas flows through the 0.2% enriched water receptacle and the samples' chemical compositions, i.e. oxygen content, change as they equilibrate with the surrounding gas mixture. The time required for this is basically determined by the oxygen chemical diffusion coefficient under these conditions. In our case, samples were left to equilibrate for approximately 15 h, far in excess of the time necessary to reach a uniform oxygen composition in the sample (based on our own electrical conductivity measurements and oxygen chemical diffusion coefficients quoted in [8]).

Once the samples have reached equilibrium, they are placed in the cold region of the furnace and stage 2 begins. The gas mixture is made to flow through the receptacle containing 98% ^{18}O enriched water. Samples are reinserted in the hot part of the furnace and annealing subsequently continues for two hours under these conditions. At the end of this period, the samples are again placed in the cold zone thus precluding any additional oxygen diffusion.

The samples were annealed at 750 °C and at an oxygen partial pressure of 2.4×10^{-22} atm. The temperature was monitored using a platinum rhodium thermocouple placed near the sample holder and the oxygen potential measured using a zirconia oxygen probe. The temperature is known to within 5 °C and the error relative to the oxygen partial pressure is estimated at 8×10^{-23} atm.

2.4. ^{18}O depth profiling

The ^{18}O penetration was characterised using a Cameca IMS 6f Secondary Ion Mass Spectrometer (SIMS) at CEA/Cadarache, where the instrument has been customised for the safe handling of radioactive materials [9]. A focussed 10 keV Cs^+ beam, with a current of ~50 nA to ~150 nA, was rastered over an area of 150 μm by 150 μm on the sample surface. Secondary ions were efficiently collected, using a 5 kV extraction field, from a smaller circular region (30 μm in diameter) located in the centre of the sputtered area in order to minimize crater-edge effects (optical gating). The primary beam current, measured at the beginning and the end of each depth profile acquisition sequence, varied over only a few nanoamperes, thus guaranteeing quasi constant sputtering rates. $^{16}O^+$ and $^{18}O^+$ ions were detected along with $^{235}U^+$ and $^{235}U^{16}O^+$ ions which are indicative of matrix sputtering rates. Several depth profiles were recorded for each sample three of which are analysed below.

Crater depths were characterised using an optical technique based on chromatic confocal microscopy developed and patented by STIL SA [10]. The system is made up of a light source, a lens also known as an optical pen, and an optoelectronic device for signal acquisition and processing. The "controller" (i.e. light source and optoelectronic device) was a CHR150 and the lens an OP20 model. The technique takes advantage of the chromatic aberration of the lens: a white light source is imaged through the lens into a continuum of monochromatic images along the optical axis of the system. When an object is present in this "coloured field", a unique wavelength is focussed at its surface and then reflected back into the system. The wavelength is then analysed using a spectrophotometer and an unequivocal correspondence can be established between the axial position of the illuminated point at the surface of the sample and the wavelength it reflects. The analysis of the spectrum of light reflected at the surface thus provides the topological information sought. The system can provide depth measurements with an accuracy of up to ±10 nm. Under the experimental conditions applied, the accuracy was estimated at ±17 nm. The light spot roughly 3 μm in diameter was rastered in 2 μm steps in both *X* and *Y* directions over areas typically of 1.5 mm by 1.5 mm containing the craters to be characterised.

3. Results

3.1. Electrical conductivity

Electrical conductivity measurements performed between 1000 °C and 1300 °C on a single crystal sample as a function of temperature and oxygen potential are indicated in Fig. 1.

The figure clearly reveals two conduction regimes as identified by previous authors. The first corresponds to a region in which electrical conductivity is independent of oxygen potential. In this regime, conduction in the material has been demonstrated from Seebeck coefficient measurements [11] to be insured by holes (i.e. p-type conduction) created for charge compensation reasons by impurities (hence reference to an extrinsic regime) assumed to be present on the cation sublattice and the valence of which is less than +4. At higher oxygen potential, oxidation of U^{4+} ions to a U^{5+} state proceeds as a result of the introduction in the material

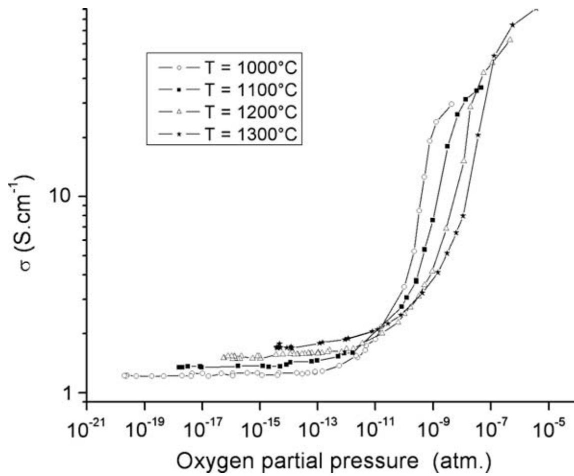

Fig. 1. Electrical conductivity of a single crystal as a function of temperature and oxygen potential.

of increasing quantities of presumably negatively charged interstitial oxygen atoms. This regime is referred to as an intrinsic regime in which the concentration of thermally produced charge carriers exceeds that due to the presence of low-valence cationic impurities. The results obtained for both sets of samples at low oxygen potential, i.e. in the extrinsic regime, are plotted in Fig. 2 which shows the data follows an Arrhenius behaviour. In addition, the data points for both sets of samples are aligned along roughly parallel lines.

3.2. Depth profiling

^{18}O relative concentrations are determined as a function of sputtering time by calculating the following ratio:

$$C(^{18}O) = \frac{N(^{18}O)}{N(^{18}O) + N(^{16}O)} \tag{1}$$

where $N(^{18}O)$ and $N(^{16}O)$ represent the count rates for $^{18}O^+$ and $^{16}O^+$ ions respectively. SIMS is ideally suited for isotopic depth profiles of atomic species that constitute the matrix (as in self-diffusion coefficient measurements) since the same chemical species is used as an internal standard for normalising the signal, thus avoiding complications associated with differences in ionisation yields between the matrix species and the species one wishes to depth profile. The accuracy associated with the ^{18}O concentration is simply obtained based on statistical fluctuations due to the number of counts. The difficulty with depth profiling lies in scaling the data obtained against depth as opposed to sputtering time. To this end, chromatic confocal microscopy is used, the result of which is shown in Fig. 3a and b in which the colour coding corresponds to the altitude determined at the surface of the sample.

Raw images are straightened and areas around the craters selected as representing the surface. A circular area approximately 60 μm in diameter is selected from within the crater and a depth histogram generated from points lying at the surface of sample and points at the bottom of the SIMS crater. Selecting a 60 μm diameter area guarantees that the estimated sputtering rate corresponds to a zone that actually covers the area from which the SIMS signal is collected (i.e. a 30 μm circular zone).

Typical histograms for a single and polycrystalline sample are shown in Fig. 4a and b.

The depth distributions corresponding to points at the surface of the samples are much broader than the 17 nm accuracy alluded to previously. Also, it should be noted that the depths corresponding to the bottom of the crater are very widely distributed. There are basically three contributing factors to the degradation of the depth resolution in SIMS. The first is associated with the initial sur-

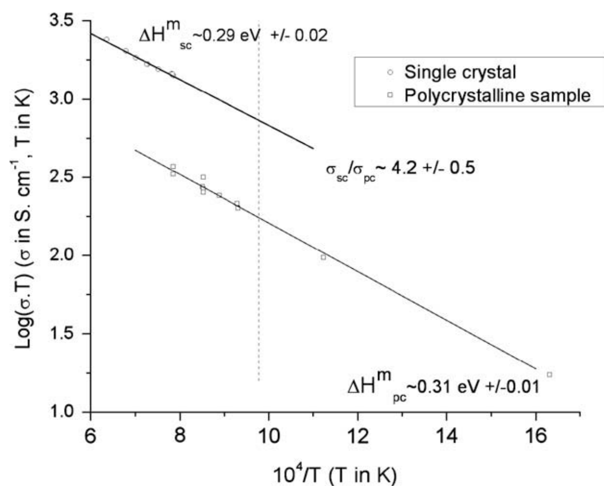

Fig. 2. Electrical conductivity measurements performed on single crystal and polycrystalline specimens in an extrinsic conduction regime.

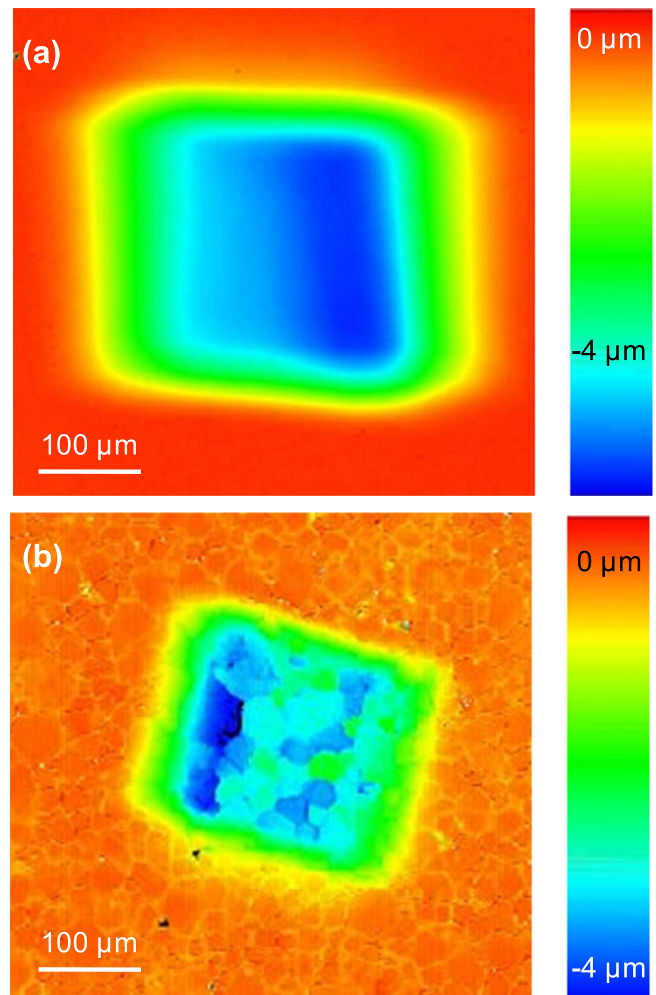

Fig. 3. Colour coded images of SIMS craters obtained using chromatic confocal microscopy for single crystal (3a) and polycrystalline (3b) samples. (For interpretation of the references to colour in this figure legend, the reader is referred to the web version of this article.)

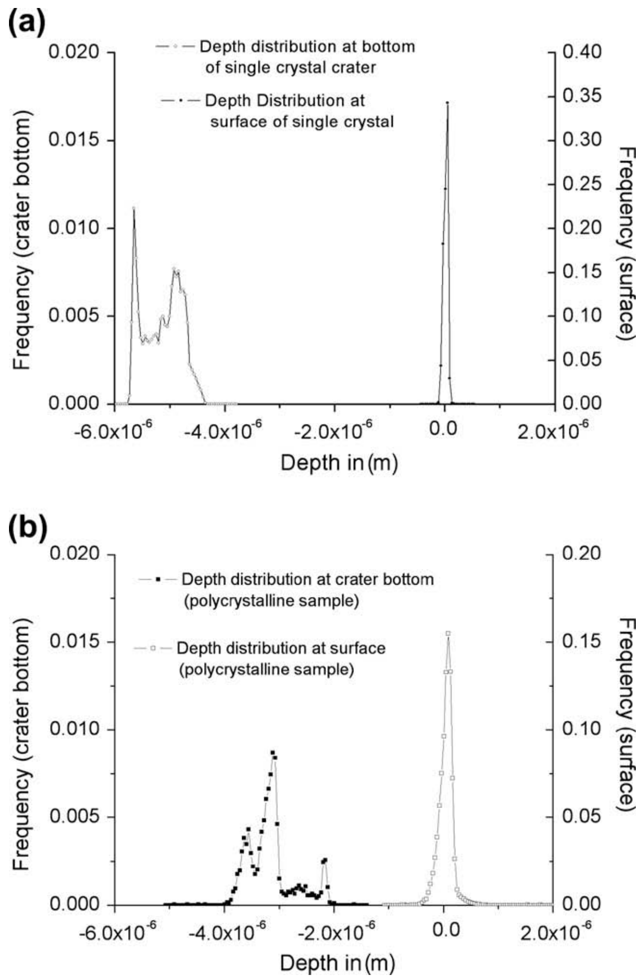

Fig. 4. Depth distributions at the bottom of SIMS craters and at the surface of the samples for single crystal (4a) and polycrystalline (4b) specimens.

face roughness of the samples. As can be seen from Fig. 4b, the situation is compounded in the case of polycrystalline samples which were annealed at high temperature prior to experimentation. This caused the grain boundaries to be revealed and characteristic furrows to appear in regions at the interface and immediately surrounding two contiguous grains. The second results from surface roughness developing at the bottom of the craters as a result of the sputtering process. The third and most important in our case induces the bottom of the crater to slant to one side. This latter phenomenon could no doubt be minimised by working at smaller primary beam currents which is conducive to obtaining small beam sizes. One can also reasonably assume from Fig. 3b, that sputtering rates in UO_2 are strongly dependent upon grain orientation which further deteriorates the depth resolution in the case of polycrystalline samples.

In order that an estimate of the accuracy associated with the relevant physical parameters (i.e. diffusion coefficients and surface isotopic exchange parameters) be determined, careful attention must be paid to depth resolution. If the crater depths were determined with infinite accuracy and if the crater bottom lay in a plane parallel to the surface, sputtering time t_s and depth z would simply be related as follows:

$$z = v_p \cdot t_s \tag{2}$$

where v_p is the sputtering rate assumed to be constant throughout the analysis. The only physical value to which an uncertainty should be associated would be the ^{18}O concentration. In order to account for the roughness both at the sample surface and at the bottom of craters and for the fact that the crater bottom appears to be slanting, one must consider the depth distributions illustrated in Fig. 4. This is done using a Monte-Carlo method. Firstly, the depth distributions at the surface of the sample and the bottom of the craters are convoluted so that the distribution of sputtering rates can be determined. Then, a sequence of sputtering rates is drawn in such a way that the distribution associated with that random variable follows the experimentally determined distribution of sputtering rates. Using Eq. (2), depth profiles can be generated for each randomly drawn sputtering rate and an average depth profile determined for each crater analysis, as illustrated in Fig. 5. This figure indicates results relative to three SIMS analyses, i.e. three craters, carried out on each of the two samples studied in the diffusion experiment (single crystal and polycrystalline sample).

4. Discussion

4.1. Electrical conductivity

Firstly, note that the temperature dependent data indicated in Fig. 2 were obtained under atmospheres such that the electrical conductivity of the samples was independent of oxygen potential. Therefore following the analysis of Ruello et al. [11], one must conclude that under these temperature and oxygen potential conditions, impurities in both sets of samples control the hole or h° concentration and hence determine the material's electrical con-

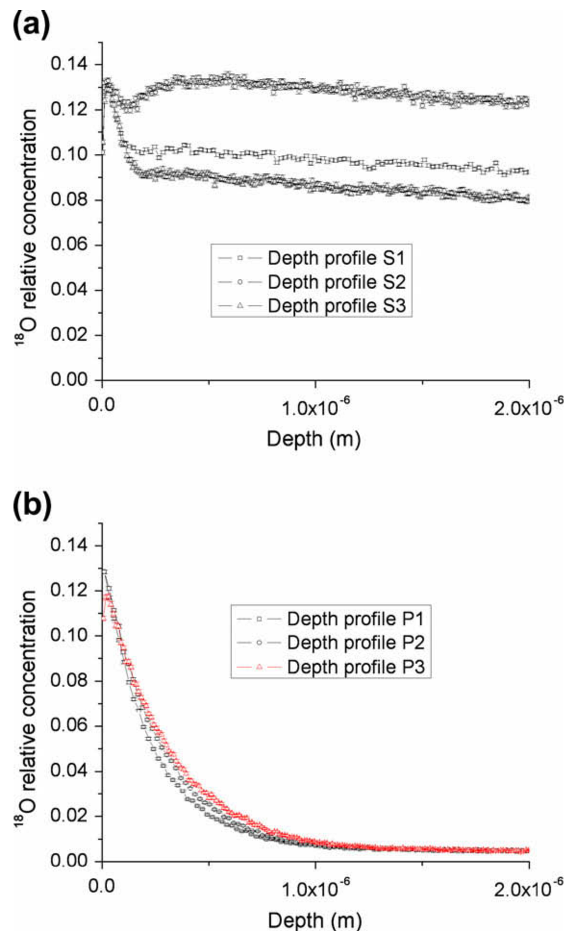

Fig. 5. Depth profiles obtained using an average sputtering rate for single crystal (5a) and polycrystalline (5b) specimens.

ductivity. The temperature dependent data in this "extrinsic" p-conduction regime can be analysed assuming the hopping mechanism to be adiabatic (this is the case when the charge jump frequency lies well above the lattice vibration frequency). In this case the electrical conductivity of the material as a function of temperature may be expressed as:

$$\sigma \cdot T = e \cdot \mu^p \cdot [h^\circ] = e \cdot \mu_o^p \cdot e^{\frac{-\Delta H_p^m}{k_b \cdot T}} [h^\circ] \quad (3)$$

where e represents the charge of an electron and μ^p, the hole mobility and ΔH_p^m the charge migration enthalpy. Fig. 2 shows that the experimental data does indeed follow the expression given by Eq. (3). The migration enthalpy (~0.3 eV) deduced from the data analysis for both sets of samples is close to previously reported values [6,7]. Further assuming μ_o^p to be in the region of 554 (in $cm^2\,V^{-1}\,s^{-1}\,K$) as suggested previously [6], enables the charge carrier concentration formed for charge compensation reasons on the cation sublattice to be evaluated. The analysis of the data shows this concentration to be $6.7 \pm 0.6 \times 10^{19}\,cm^{-3}$ and $2.3 \pm 0.3 \times 10^{20}\,cm^{-3}$ for the polycrystalline and single crystal samples studied. Chemical analyses of the single crystals revealed the presence of Cr, Ni, Fe, Mn, Ca. From these analyses the charge carrier concentration could be evaluated at between 1.3 and $1.7 \times 10^{20}\,cm^{-3}$, depending on the charge state of Fe ions. A similar analysis of polycrystalline samples yields a charge concentration one order of magnitude lower than that deduced from electrical conductivity measurements. However, common impurity atoms such as calcium were not looked for in the chemical analysis but were shown from SIMS analyses to be present, although no quantitative data could be produced.

4.2. ^{18}O Depth profiles

4.2.1. ^{18}O contamination of the setup

In this type of isotopic exchange experiment, if intrinsic diffusion only is involved, one would expect the ^{18}O concentration profile to follow an analytical solution to Fick's equation involving the complementary error function (see [1] for instance), with the concentration towards the end of the profile falling to a value equal to the natural abundance of ^{18}O atoms (i.e. 0.2%). This is clearly not the case for concentration profiles shown in Fig. 5a or b. Depth profiles relative to the single crystal samples in particular can clearly not be reproduced using a simple analytical solution to Fick's second law and in both the single crystal and polycrystalline cases, the ^{18}O concentration towards the tail end of the profile does not drop to the expected 0.2% value. This suggests that several other phenomena were occurring during our experiments which we will now attempt to analyse in the light of sample preparation and experimental details.

We focus on depth profiles relative to the single crystal. It is suggested that the high ^{18}O levels in the bulk of the sample, come about during the pre-annealing stage (stage 1 in Section 2.3) of the experiment as a result of an ^{18}O contamination of the setup from previous diffusion experiments. During this first stage of the annealing experiment, samples are brought to equilibrium with the oxygen partial pressure of the carrier gas which flows through a receptacle containing $H_2^{16}O$ only. However, ^{18}O atoms are released from the inner surfaces of the quartz tube resulting in contamination of the samples. Because the oxygen content of the samples is changing during this stage of the process, the kinetics of sample contamination is expected to be high (as suggested from the long tail end of all depth profiles) since prescribed by the oxygen chemical diffusion coefficient. Ruello et al. [8] have measured this property in an oxygen composition range (deviation from stoichiometry) which lies between $x \sim 0.03$ and $x \sim 0.17$. At 750 °C, the chemical diffusion coefficient may be extrapolated to values ranging between $6 \times 10^{-13}\,m^2/s$ and $10^{-11}\,m^2/s$. An analytical solution to the diffusion equation (i.e. Fick's second law) may be fitted to the tail end of the profiles such as those indicated in Fig. 5a. This exercise yields what is interpreted as a chemical diffusion coefficient which lies between $10^{-13}\,m^2/s$ and $10^{-14}\,m^2/s$ depending on whether the time for the sample to reach an equilibrium oxygen composition is 15 min or 3 h respectively (corresponding roughly to the time it takes for the electrical conductivity to reach a stable value). In this numerical application, the ^{18}O concentration in the gas phase is assumed constant and equal to 20%. The values obtained for chemical diffusion coefficients are not very sensitive to this parameter.

The fact that the ^{18}O concentration levels in the bulk of the single crystal are heterogeneous, but that the concentration profiles are roughly parallel, suggests a – that the composition in the bulk of the sample prior to the equilibrium pre-annealing was homogeneous (since the slope of the profile is mainly dependent upon the diffusion coefficient) and b – that the surface of the samples were not (the concentration level at the surface is mostly dependent upon the isotopic exchange coefficient). Profile S2 is particularly interesting: it suggests that ^{18}O contamination during pre-annealing comprises two stages. During the first stage, due to the initially high levels of ^{18}O contamination, ^{18}O penetrates the material whose oxygen composition is changing. As pre-annealing continues, the ^{18}O concentration level in the gas phase continuously decreases and the ^{18}O concentration at the sample surface begins to decrease accordingly with kinetics determined by the intrinsic oxygen diffusion coefficient (several orders of magnitude smaller than the chemical diffusion coefficient). This latter phenomenon therefore affects an area much closer to the surface of the material than the chemical diffusion process, as seen in Fig. 5a.

4.2.2. Comparison between bulk ^{18}O concentrations in both samples

It is also necessary to address the issue of why the oxygen concentration in the bulk of the polycrystalline sample is so much lower than that in the single crystals. The reason for this is to be found in the way the samples were manufactured and prepared. Recall that the single crystal specimens were cut in a bloc of molten UO_2. These were obtained from fusion experiments in which samples containing uranium dioxide pellets in a zirconium cladding were melted down at very high temperature. It is reasonable to suggest that the oxygen potential during the melting process and as the material solidified was imposed by the Zr/ZrO_2 couple. These conditions were likely favourable to forming sub-stoichiometric uranium dioxide upon cooling. Initially, the single crystals were therefore probably highly deficient in oxygen. When they were brought to equilibrium (first stage of the annealing process), they incorporated much greater amounts of oxygen than the polycrystalline material. ^{18}O was thus incorporated in large quantities because of its availability due to the experimental caveat described in the previous section. By contrast, the polycrystalline samples were all pre-annealed before any diffusion experiment at 1700 °C in a reducing atmosphere (Ar/4% H_2) and one can reasonably assume that they were much closer to a stoichiometric composition when they were initially introduced in the furnace. The samples were exposed to the same quantities of ^{18}O that was not incorporated to the polycrystalline sample because it was not as deficient in oxygen as the single crystal.

4.2.3. Quantitative data analysis

From the two previous sections, it appears that our experiments comprise three steps, only two of which are clearly seen on all depth profiles:

1. During stage 1 of the annealing experiment, ^{18}O atoms left over from previous experiments contaminate the samples at a high rate, determined by the oxygen chemical diffusion coefficient.

2. The concentration at the surface of the samples then drops to low values as ^{18}O atoms become less available. Because the samples are at this stage at equilibrium with the carrier gas, this process is much slower and governed by the oxygen self-diffusion coefficient.
3. During stage 2 of the annealing procedure, the ^{18}O concentration at the surface of sample rises slowly over the two-hour annealing period at a rate consistent with the oxygen self-diffusion coefficient.

Despite these experimental complications, it is possible to derive physical parameters characteristic of the materials studied based on an analysis of all three steps outlined above. The initial ^{18}O concentration is obtained by extrapolating back to the surface the tail end of the depth profile, thus accounting for step 1. Application of Fick's second law to the evolution of the initial profile is done over a period of approximately 12 h, during which the ^{18}O concentration in the gas phase (C_g) is assumed to be zero (description of step 2). The equation and boundary condition problem to be solved can be expressed as follows:

$$\begin{aligned} &\partial C^{18}O = \frac{\partial}{\partial z}\left(D\frac{\partial C^{18}O}{\partial z}\right) \\ &D\cdot\left(\frac{\partial C^{18}O}{\partial z}\right)_{z=0} = -k(C_g - C(0)) \end{aligned} \tag{4}$$

with obvious notations and where D and k are the intrinsic oxygen diffusion coefficient and the isotopic exchange coefficient respectively. The intrinsic diffusion coefficient is finally quantified from fitting the physical parameters in Eq. (4) to the experimental data under conditions corresponding to an ^{18}O concentration in the gas phase of 98% and for a two hour period (quantitative description of step 3). The accuracy associated with the determination of physical parameters D and k is estimated by fitting model parameters to depth profiles obtained from the random generation of sputtering rates. The sputtering rates are generated in such a way that they follow the experimentally determined sputtering rate distribution as previously described. D and k values are obtained from fitting 20 depth profiles for each SIMS crater. Examples of how the model fits the experimental data are given in Fig. 6a and b. When relevant, the depth profile following pre-annealing and just before the gas phase is loaded with ^{18}O is indicated (crater S2). Table 1 summarises the intrinsic diffusion and isotopic exchange coefficients obtained at a temperature of 750 °C and a partial pressure of 2.4×10^{-22} atm.

The results indicated in Table 1 show that the values derived from this analysis are extremely consistent for data pertaining to the same sample despite considerable differences in the bulk ^{18}O concentrations. Also, both the isotopic exchange and the diffusion coefficients are an order of magnitude greater in polycrystalline samples in which the charge carrier concentration is four times smaller. This indicates a strong correlation between charge carrier and point defect concentrations. The diffusion coefficient values are similar to those obtained by other authors ([12,13]) for nominally stoichiometric UO_2. Differences probably stem from the oxygen potentials the samples were subjected to and the level and nature of impurities the materials contained, neither of which have been reported quantitatively in previous studies.

4.3. Application of a point defect approach for data interpretation

In order to investigate this point further, we turn to diffusion theory. Assuming oxygen diffusion proceeds either via interstitial or vacancy defect migration in UO_{2+x}, the intrinsic oxygen diffusion coefficient may be expressed as:

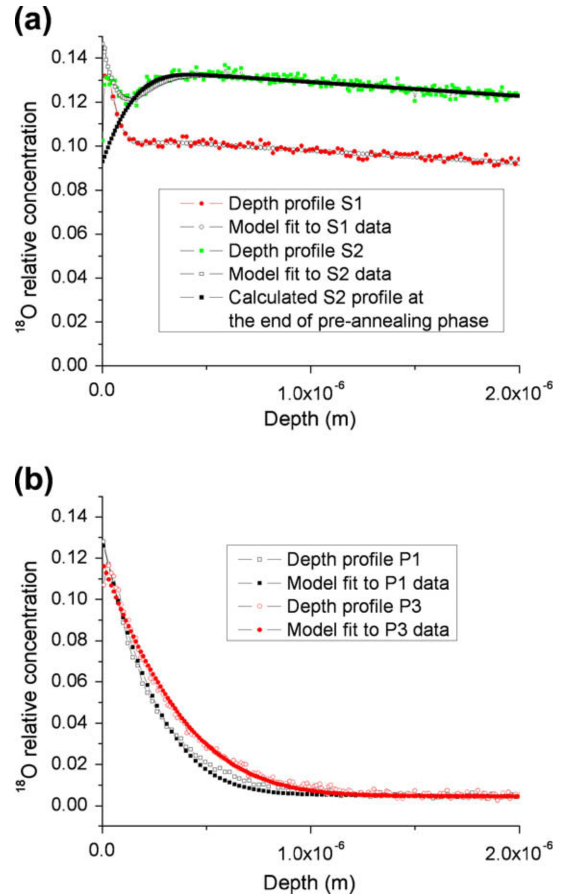

Fig. 6. Comparison of model calculation results to experimental data for single crystal (6a) and polycrystalline (6b) specimens.

Table 1
Intrinsic diffusion and isotopic exchange coefficients obtained from the analysis of three SIMS datasets for each of the two samples studied.

Profile	D (m²/s)	k (m²/s)
S1	$5.4 \times 10^{-19} \pm 10^{-19}$	$4.8 \times 10^{-13} \pm 6 \times 10^{-14}$
S2	$6.4 \times 10^{-19} \pm 1.6 \times 10^{-19}$	$3.2 \times 10^{-13} \pm 4 \times 10^{-14}$
S3	$7.6 \times 10^{-19} \pm 10^{-19}$	$7.6 \times 10^{-13} \pm 8 \times 10^{-14}$
P1	$1.0 \times 10^{-17} \pm 3 \times 10^{-18}$	$4.5 \times 10^{-12} \pm 7 \times 10^{-13}$
P2	$1.4 \times 10^{-17} \pm 3 \times 10^{-18}$	$5.3 \times 10^{-12} \pm 6 \times 10^{-13}$
P3	$1.8 \times 10^{-17} \pm 2 \times 10^{-18}$	$5.7 \times 10^{-12} \pm 4 \times 10^{-13}$

$$D_O \propto [O_i''] \cdot e^{\frac{-\Delta H_m^{O_i}}{k_b T}} + [V_O^{\circ\circ}] \cdot e^{\frac{-\Delta H_m^{V_O}}{k_b T}} \tag{5}$$

where $[O_i'']$ and $[V_O^{\circ\circ}]$ represent the oxygen interstitial and vacancy concentrations. Let us further assume that oxygen interstitials and vacancies are both doubly charged. Using the Kröger Vink notation, mass balance equations may be established which express thermodynamic equilibrium between charge carriers and point defects:

$$O_X \rightleftharpoons O_i'' + V_O^{\circ\circ} \tag{6}$$

$$\frac{1}{2}O_2 \rightleftharpoons O_i'' + 2\cdot h^{\circ} \tag{7}$$

The corresponding equilibrium constants, dependent upon temperature only, can then be written as:

$$K_{AF} = [O_i''] \cdot [V_O^{\circ\circ}] \tag{8}$$

$$K_{O_i} = \frac{[O_i''] \cdot [h^{\circ}]^2}{\sqrt{p(O_2)}} \tag{9}$$

Combining Eq. (5) with Eqs. (8) and (9) yields the following expression for the oxygen diffusion coefficient:

$$D_O \propto \frac{1}{[h^\circ]^2} \cdot \sqrt{p(O^2)} \cdot K_{O_i} \cdot e^{\frac{-\Delta H_m^{O_i}}{k_b T}} + [h^\circ]^2 \cdot \frac{K_{AF}}{K_{O_i}} \cdot \frac{1}{\sqrt{p(O_2)}} \cdot e^{\frac{-\Delta H_m^{V_O}}{k_b T}} \tag{10}$$

Therefore at a given oxygen potential and temperature, the oxygen diffusion coefficient will either vary proportionally to the square of the hole concentration or as one over this quantity depending on whether migration occurs predominantly via an interstitial or vacancy mechanism.

We now seek to ascertain whether our experimental data corroborates this simple theory. From Table 1, it is possible to give an estimate of the quantity:

$$r = \sqrt{\frac{D_O^{pc}}{D_O^{sc}}} \tag{11}$$

Using the rule of propagation of errors, r is estimated at 4.7 ± 0.6. From electrical conductivity measurements, it is possible to estimate the ratio between the charge carrier concentration at 750 °C in single crystals and polycrystalline samples. This ratio is estimated at 4.2 ± 0.5. Both these values are remarkably close which indicates D_O varies as $1/h^{\circ 2}$ thus emphasising the relevance of Eq. (10).

The conclusions to be drawn from this are extremely important: in the extrinsic regime investigated here and assuming holes bear a single positive charge, oxygen migration proceeds via doubly charged oxygen interstitials. This does not preclude the existence of other point defects; however, they do not appear to interfere with the migration process.

Attention is now turning to the dependence upon temperature and oxygen potential of the diffusion coefficient in order that the relevance of Eq. (10) may be further demonstrated and that oxygen migration energies and free energies associated with the defect equilibria may be measured.

5. Conclusions

In this work, we have characterised the electrical conductivity and oxygen diffusion properties of two different sets of samples to determine the nature of point defects responsible for oxygen migration in uranium dioxide. We have shown that in the extrinsic region studied (750 °C and oxygen partial pressure of 2×10^{-22} atm), oxygen interstitials are the point defects responsible for atomic migration. Confrontation of experimental results with basic point-defect theory suggests that these oxygen interstitials are doubly charged. The consequence is that aliovalent impurities with a charge of +2 or +3, present on the cation sublattice control oxygen point defect concentrations in UO_2. Future work will include exploring broader ranges of temperature and oxygen partial pressures in order to substantiate these results. On a more general note, we show that combining these two techniques under very different thermodynamic conditions has the potential to enable the construction and validation of a comprehensive and to date elusive point defect model for UO_2.

Finally this type of work will provide invaluable data for validating first principle electronic structure calculations such as migration energies of point defects of a given nature along with free energies associated with the mass balance equations which govern the system.

Acknowledgment

This work was partly sponsored by the European Commission through the FP7 F-BRIDGE project (Contract No. 211690).

References

[1] J. Philibert, in: Atom Movements – Diffusion and Mass transport in Solids, Editions de Physique, Les Ulis, 1991.
[2] G.E. Murch, C. Richard, A. Catlow, J. Chem. Soc., Faraday Trans. 2 (83) (1987) 1157.
[3] A.C.S. Sabioni, W.B. Ferraz, F. Millot, J. Nucl. Mater. 278 (2000) 364.
[4] R. Dieckmann, Solid State Ionics 12 (1984) 1.
[5] C. Dubois, C. Monty, J. Philibert, Philos. Mag. A 46 (1982) 419.
[6] N.J. Dudney, R.L. Coble, H.L. Tuller, J. Am. Ceram. Soc. 64 (1981) 627.
[7] P. Ruello. Etude du Changement de Comportement du Dioxyde d'Uranium au Voisinage de 1300 K, Thesis, E.C.P., 2001.
[8] P. Ruello, G. Ghirlesan, G. Petot-Evras, C. Petot, L. Desgranges, J. Nucl. Mater. 325 (2004) 202.
[9] L. Desgranges, B. Pasquet, Nucl. Instrum. Methods B 215 (2004) 545.
[10] Information on <http://www.stilsa.com>.
[11] P. Ruello, G. Petot-Evras, C. Petot, J. Am. Ceram. Soc. 88 (2005) 604.
[12] J.F. Marin, P. Contamin, J. Nucl. Mater. 30 (1969) 16.
[13] A.B. Auskern, J. Belle, J. Nucl. Mater. 3 (1961) 267.